Toward Medical Devices With Integrated Mechanisms, Sensors, and Actuators Via Printed-Circuit MEMS

Share Your Story

Towards Medical Devices with Integrated Mechanisms, Sensors and Actuators via Printed-Circuit MEMS

Joshua Gafford[1] [*], **Tommaso Ranzani**[2], **Shiela Russo**[2], **Alperen Degirmenci**[1],
Samuel Kesner[2], **Robert Howe**[1,2], **Robert Wood**[1,2], **Conor Walsh**[1,2]
[1]John A. Paulson School of Engineering and Applied Sciences, Harvard University
[2]Wyss Institute for Biologically-Inspired Engineering
Cambridge, MA 02138
*Email: jgafford@seas.harvard.edu

Recent advances in medical robotics have initiated a transition from rigid serial manipulators to flexible or continuum robots capable of navigating to confined anatomy within the body. A desire for further procedure minimization is a key accelerator for the development of these flexible systems where the end goal is to provide access to previously inaccessible anatomical workspaces and enable new minimally-invasive surgical (MIS) procedures. While sophisticated navigation and control capabilities have been demonstrated for such systems, existing manufacturing approaches have limited the capabilities of mm-scale end-effectors for these flexible systems to date and, to achieve next generation highly-functional end-effectors for surgical robots, advanced manufacturing approaches are required. We address this challenge by utilizing a disruptive 2D layer-by-layer precision fabrication process (inspired by printed circuit board manufacturing) that can create functional 3D mechanisms by folding 2D layers of materials which may be structural, flexible, adhesive, or conductive. Such an approach enables actuation, sensing and circuitry to be directly integrated with the articulating features by selecting the appropriate materials during the layer-by-layer manufacturing process. To demonstrate the efficacy of this technology, we use it to fabricate three modular robotic components at the millimeter-scale: (1) sensors, (2) mechanisms, and (3) actuators. These modules could potentially be implemented into transendoscopic systems, enabling bilateral grasping, retraction and cutting, and could potentially mitigate challenging MIS interventions performed via endoscopy or flexible means. This research lays the ground work for new mechanism, sensor and actuation technologies that can be readily integrated via new mm-scale layer-by-layer manufacturing approaches.

---

[*]Address all correspondence related to ASME style format and figures to this author.

1 Introduction

A key trend in surgical robotics that has been accelerating innovation in recent years is a desire to reduce the scale, cost and complexity of surgical robotic systems in particular as there has been an increased emphasis on reducing procedure invasiveness and associated healthcare costs [1]. This trend is driving innovation in flexible robotic systems and co-robotic, smaller-scale systems capable of performning LESS (laparoendoscopic single-site surgery) and NOTES (natural orifice transluminal endoscopic surgery). As a result, surgical robotics is shifting away from more traditional rigid telerobotic master-slave paradigms that are designed for larger, more accessible anatomical workspaces. [2, 3, 4, 5].

Flexible robotic systems, due to their inherent dexterity and ability to access confined regions within the body, are seen as potential enablers for more advanced MIS techniques in a number of burgeoning MIS arenas (neurological, gastrointestinal, pulmonologic and urologic to name a few). However, despite significant advances in the design, modeling and control of flexible and continuum surgical robot platforms [6], existing manufacturing approaches have limited the sophistication of mm-scale end-effectors to date, ultimately limiting the performance, applicability, and widespread adoption of these systems. Typical end-effector implementations demonstrated in literature for flexible platforms include simple cable-driven forceps actuated by off-board motors, passive devices such as blades and curettes, and energy delivery devices (such as RF ablation and electrocautery) which require no mechanical force transmission [7, 8]. Limitations in achievable complexity and a reliance on traditional approaches to end-effector design and manufacturing ultimately limit the therapeutic capabilities of these flexible systems. Furthermore, the compliant nature of these flexible systems brings about a number of challenges that call for more advanced end-effectors, including (1) difficulties in transmitting substantial forces distally for tissue manipulation and removal, and (2) the inability to use off-board sen-
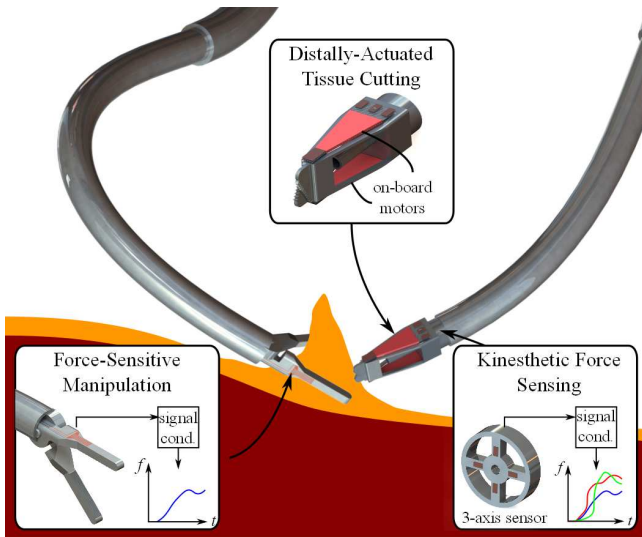
Fig. 1. Conceptual LESS dissection procedure, with callouts illustrating end-effector modules developed in this research.

sors for force estimation.

1.1 State-of-the-art

Achieving the next generation of highly-functional end-effectors for surgical robots, such as those shown in Fig. 1, will require advanced manufacturing approaches. One approach to this problem uses a novel metal MEMS microfabrication technique to develop mm-scale metal devices out of several engineering-grade metal alloys [9]. Other groups have used silicon-based MEMS [10] and additive manufacturing processes [11] to build devices at scale. Despite these advances, it remains a significant challenge to integrate electronics, sensors and actuators into mechanical substrates to develop low-cost, 3-dimensional electromechanical systems at mm-scales. We address this challenge by utilizing a disruptive 2D layer-by-layer precision fabrication process (inspired by printed circuit board manufacturing) called PCMEMS (printed-circuit MEMS) that can create functional 3D mechanisms by folding 2D layers of materials which may be structural, flexible, adhesive, or conductive [12]. Linkages and hinges are machined and integrated into a laminate that fold in concert, like the pages of a pop-up book, to enable self-assembly into a 3D mechanism from a 2D laminate. In addition to structural/flexible layers that guide kinematics, other type of materials, such as actuating (i.e. piezo-electric) and sensing (i.e. strain gage alloy) materials, can be directly integrated with the articulating features by selecting the appropriate material during the layer-by-layer manufacturing process.

As flexible surgical robots continue to develop, focus must shift towards novel end-effector developments that will enable more complex procedures. Highly miniaturized end-effectors with integrated articulation, sensing and actuation will create new possibilities for cooperative control strategies for such tools where a lower-level loop is closed dis-

tally based on information from on-board sensor/actuator system. Benefits of distal loop closure include (1) control loop stability (distal sensors and actuators have direct access to the anatomy and are not corrupted by unknown proximal forces), (2) footprint reduction of back-end infrastructures (off-board actuators) that clutter the surgical arena, and (3) the opportunity to develop a new class of task-specific, hand-held co-robotic tools where low-level tasks can be automated and performed at the end-effector level (for example, force-controlled cutting, tissue discrimination via mechanical or electrical biomarkers, or contact-modulated energy delivery).

1.2 Contribution

This paper serves to draw lessons that can be generalized across mechanisms, sensors, and actuators so that the work can be viewed holistically to understand the challenges that remain in using this fabrication process to develop surgical tools that are suitable for clinical use. We also analyze the process as a viable means of producing low-cost medical devices and robotic modules by addressing process economy, biocompatibility and sterilizability concerns. We begin with a discussion of the manufacturing process itself and how it can be used to fabricate fully-integrated electromechanical devices. We then present demonstrative examples in which PCMEMS was used to build a fully-functioning mm-scale medical device prototype that fits under the umbrella of at least one of the aforementioned modular components. The first example highlights several force sensors manufactured via PCMEMS, each employing a different transduction modality (strain gage, light-intensity modulation and capacitance). The second example demonstrates a microsurgical forceps with integrated grip force sensing which can be used for precision manipulation of delicate tissue. The third example demonstrates a high-frequency soft-tissue cutting device actuated by on-board piezoelectric elements. We conclude with a discussion of some technical and practical limitations of this technique, as well as recommendations for future work.

2 Manufacturing Overview

A notable contribution of this work is the appropriation of disruptive fabrication techniques to build complicated mechanisms and devices at the micro/meso-scale. Originally developed to manufacture and self-assemble millimeter-sized crawling and flying robots, PCMEMS is a manufacturing process that combines numerous functional material layers (including structural, flexible, adhesive, electrically/thermally conducting, insulating, actuating, etc.) into a 2-dimensional layup [12]. When laminated and released, the layup can form a 3-dimensional mechanism as determined by the kinematics of pre-machined linkages and hinges which fold in concert to 'pop' the structure out of the 2-dimensional machining plane, much like the pages of a pop-up book (Fig. 2). This capability enables the use of fast, high-tolerance laser machining processes to develop complicated
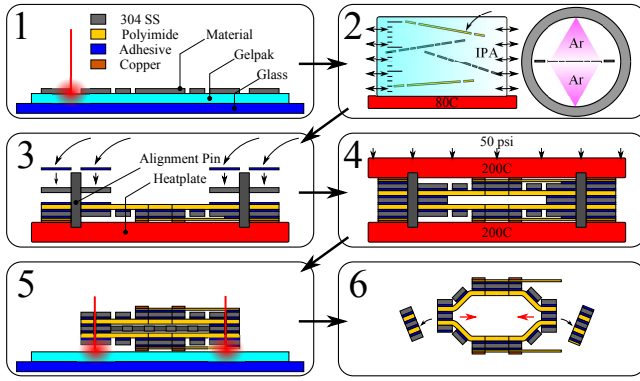
Fig. 2. PCMEMS layer-by-layer manufacturing process.

mechanisms with integrated kinematics, sensing, and actuation. The device comes out of fabrication fully assembled, obviating the need for post-fabrication assembly, bonding, and alignment. Given the capabilities of this process at manufacturing at-scale components, it is important to understand the strengths and limitations from a process economy standpoint.

2.1 Process Economy

An overview of the fabrication process, illustrated in Fig. 2, is as follows:

(1) **Initial Cuts** made in a custom-built diode-pumped solid-state (DPSS) Nd:YVO$_4$ laser, q-switched and frequency tripled to 355 nm. Galvonometer speed and frequency are dependent on the material properties.

(2) **Cleaning and Surface Treatment** via immersion in isopropanol in an ultrasonic bath at 80C for 10 minutes, followed by an etching process in Argon plasma (4 sccm, 100% forward current for 1 minute).

(3) **Stacking and Tacking** using a custom weight press and a Watlow temperature controller. Flash-curing (50 psi (345 kPa), 130C for one minute) to deposit adhesive layers onto structural layers.

(4) **Full Cure** at 50 psi, 200C for two hours.

(5) **Release Cuts** made in the DPSS laser to release part from sacrificial scaffolding material.

(6) **Feature-Guided Assembly** into the final three-dimensional mechanism.

In terms of process economy, the fabrication time scales roughly with the number of layers N included in the laminate. Cleaning, plasma etching, and adhesive tacking are batch processes (with batch sizes given by n_{etch} and n_{tack}), and curing time τ_{cure} is roughly independent of the number of layers in the laminate. As such, these processes are relatively invariant regardless of device complexity. The initial and final laser cutting processes suffer the largest dependence on device complexity, as shown in Fig. 3. The DPSS laser can be modeled as a pulsed Gaussian beam which suffers an exponential loss in power transfer and ablation rate as material is removed $\left(P \propto P_0(1 - e^{-1/\delta^2}) \right)$ (assuming the beam is focused on the top-of-stock). This can be corrected to a

point by displacing the focal depth as subsequent cut passes are made, but energy diffusion into the sidewalls ultimately limits the total depth-of-cut. Despite the decaying exponential relationship between material depth δ and ablation rate h which can drive up fabrication time for thicker materials, the true process bottleneck lies in the lamination/curing cycle which requires a fixed cure time τ_{cure}, but also requires no direct human intervention, and as such, opens up the possibility of streamlining and parallelization. The total processing time t can be approximated by performing a dimensional analysis on the processing variables, as given by the following:

$$
t = 2\left[n_{batch} \sum_{i=1}^{N} \left(\frac{l_i \delta_i}{he^{-\alpha\delta_i} f d_s} \right) \right] + \tau_{etch}\left\lceil \left(\frac{N}{n_{etch}} \right) \right\rceil
$$
$$
+ \tau_{tack}\left\lceil \left(\frac{N}{n_{tack}} \right) \right\rceil + \tau_{cure} + \tau_{setup} + \tau_{pp}
$$

(1)

where discrete layers in the laminate are denoted by i where $i \in (1, \cdots, N)$, n_{batch} is the number of devices in the current batch, l_i is the toolpath length (determined by the CAD package used to design the layers), α is an empirically determined energy loss constant, f is the laser pulse frequency in Hz, d_s is the laser spot size (which ranges from 5μm to 10 μm depending on the material being cut), and τ_{etch}, τ_{tack}, τ_{cure}, τ_{setup} and τ_{pp} are the (relatively invariant) times associated with fabrication steps indicated by the associated subscript (where pp is shorthand for 'pick-and-place'). Most of the processing time lies in setup (which can be streamlined), batch cycles (such as cleaning, etching and adhesive tacking) and laminate curing time, indicating an overall weak dependence on l and N (metrics of device complexity) which makes the process very amenable to rapid prototyping fabrication cycles. As such, this technology is a platform fabrication process that can be leveraged to prototype multiple new designs in parallel with a relatively short turn-around time (less than a day from start to finish).

2.2 Applicability to Medical Devices

PCMEMS fabrication features a number of characteristics that indicate its applicability to the manufacturing of surgical devices at millimeter scales.

1. The purely 2-dimensional fabrication enables batch manufacturing of numerous devices in parallel, resulting in high throughput and significantly driving down fabrication costs for single use or disposable devices.
2. Direct integration of sensors and actuators obviates post-manufacturing alignment, assembly, and bonding.
3. Motion is permitted via folding of flexure-based joints, eliminating concerns of friction and wear.
4. PCMEMS boasts an extensive material catalog encompassing numerous biocompatible materials and medical-grade alloys.

Given these indicators, the remainder of the discussion will focus on the design and manufacture of three modular com-
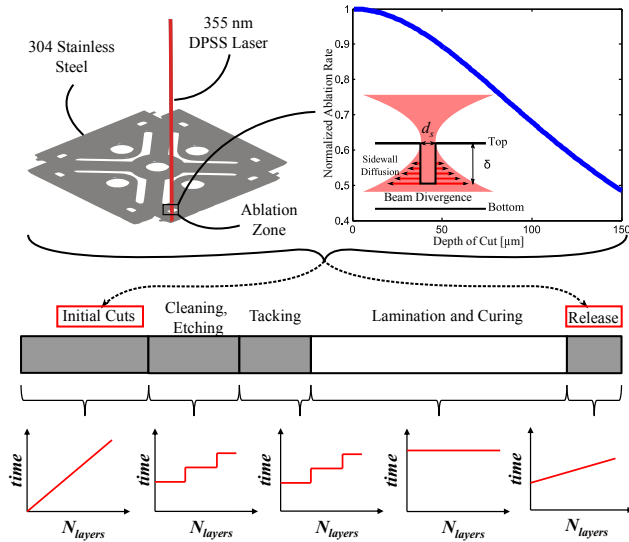
Fig. 3. (top) 355nm $Nd:YVO_4$ laser modeled as a Gaussian beam, and associated ablation rate dependence on depth of cut, (bottom) manufacturing timing diagram (hatched requires constant supervision/attention, solid requires no intervention) with qualitative graphs showing how the processing time scales with the number of layers in the laminate.

ponents with direct applications in minimally-invasive surgical robotics: (1) single- and multi-axis force sensors for haptic feedback, (2) force-sensing forceps for dexterous manipulation, and (3) distally-actuated harmonic devices for soft tissue removal.

2.3 Note on Sterilization and Usage

The ultimate goal of this work is to enable the fabrication of single-use, disposable robotic modules, which relaxes some of the requirements imposed by extended use. However, in a clinical setting, PCMEMS devices need to be robust to sterilization processes. The fabrication process necessitates a laminate curing temperature of 200 C over a duration of 2 hours. Steam sterilization entails immersion in 121 C steam for 30 minutes, followed by a 15 minute cycle at 132 C as per ISO 17665. Therefore, sterilization requirements are much less taxing on the laminate materials than the requirements of the fabrication process itself. Pre- and post-cure processes typically consists of ultrasonic cleansing in an Isopropanol bath which is a common decontamination protocol that takes place prior to sterilization. Therefore, the devices manufactured using this technique are robust to the specifications required by steam sterilization processes.

3 Sensors

As stated previously, PCMEMS has the implicit ability to integrate electrical components/sensors with mechanical substrates in a monolithic fashion. As a practical demonstration of this ability, we use PCMEMS to fabricate mm-scale single- and multi-axis force sensors for potential distal place-

ment and kinesthetic force sensing in MIS procedures.

3.1 Clinical Significance

In all MIS procedures, especially those performed robotically, the surgeon is haptically disconnected from the anatomy, and must rely on alternative cues (i.e. trained visual cues) to approximate the forces being applied by the tool onto tissue. The haptic separation manifests in the form of unregulated force application which can lead to intraoperative complications such as breaking sutures, tearing delicate tissue or perforating high-pressure vasculature, as the surgeon cannot physically 'feel' the forces being exerted by the tools that he/she is manipulating onto delicate anatomical structures [13].

Due to the size constraints imposed by MIS, a common approach to force sensing is to locate load cells or strain gages proximal to the anatomical workspace (where size limitations are relaxed) to estimate tip force based on rigid tool deflection, although these measurements are typically contaminated by normal and shear forces at the point of entry, actuation forces, and unknown forces within the body. For distal force sensing, the most straightforward implementation is to use commercial off-the-shelf (COTS) strain gages, adhered to the tool itself, to measure microstrains generated by rigid body deformation to compute the distal force [14,15]. Such an approach is not viable for flexible, catheter-based, endoscope-based and continuum systems which typically undergo large bending strains and are difficult to model using classical mechanics. Given these limitations, there is a significant body of work devoted to developing distal sensing modalities. Several groups have employed optical modalities (Fiber-Bragg gratings, Fabry-Perot interferometry or light intensity modulation) to detect tip forces, and light intensity modulation has even acquired FDA approval as a sensing modality for contact force sensing in ablation catheters [16,17,18,19]. However, these systems are susceptible to thermal drift (although a biasing fiber can be added to compensate) and often require expensive and complicated interrogators, amplifiers and filters to convert the measurand into a meaningful signal. Additionally, they require optical fibers to run along the entire length of the tool, thereby reducing modularity and occupying valuable space that could otherwise be used for working ports.

In general, designing and manufacturing cost-effective sensors that can be integrated into millimeter-scale device end-effectors is a significant challenge that conventional approaches to manufacturing and assembly are ill-suited for. As such, there is an opportunity to explore alternative means of fabricating distally-placed sensor modalities that can provide true measurements of tissue interaction forces on-board flexible delivery systems. In order to demonstrate the efficacy of PCMEMS to produce high-quality force sensors, we explore three different transduction mechanisms: (1) gage-based strain sensing, (2) light-intensity modulation-based sensing, and (3) capacitance sensing.

Analytical and Numerical Modeling
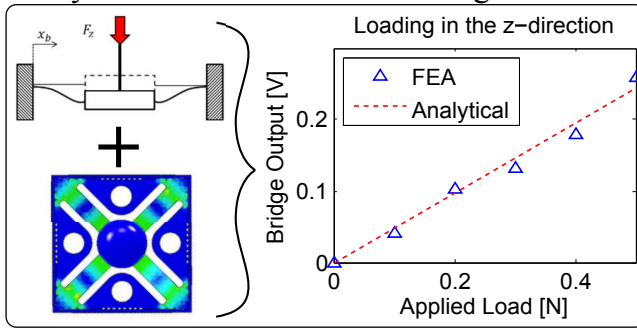
CAD Generation
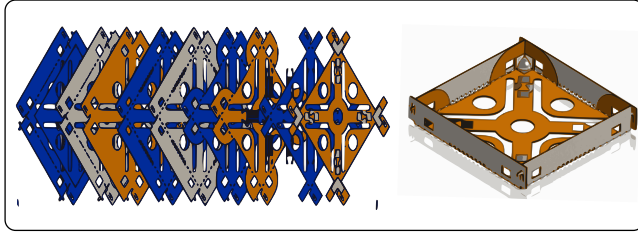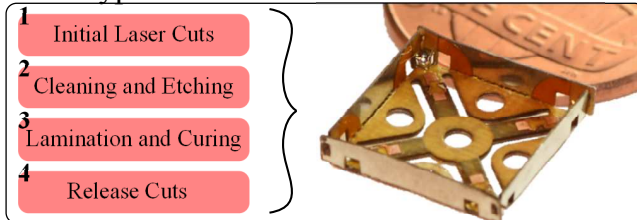

Prototype Fabrication

Fig. 4.   Deterministic design and analysis process flow used to build three-axis PCMEMS force sensor, *(top)* numerical and analytical modeling of simplified structure, *(middle)* CAD generation of tool-paths, *(bottom)* fabrication using process outlined in *Section 2.1*.

3.2   PCMEMS Sensor Design

PCMEMS sensor design and fabrication, illustrated in Fig. 4, invariably begins with a simplified analytical model of the transduction phenomena, coupled with any mechanical/kinematic models of the sensor structure itself. More complicated morphologies may necessitate numerical finite-element simulations of the proposed sensor structure to ultimately derive the electromechanical transfer function relating sensor output $\mathbf{s} \in \mathbb{R}^k$ (where k is the sensor output dimensionality) and the applied force $\mathbf{F} \in \mathbb{R}^m$ (where m is the dimensionality of the force vector being measured). These models are optimized numerically or through brute force to determine geometric parameters from application-specific functional requirements. The sensor structure itself is designed using a bottom-up approach wherein individual functional layers of material (structural, adhesive, insulating, and conducting) are designed and combined into functional sub-laminates (i.e. mechanical substrate, printed circuit, gage pattern), which ultimately combine to form the master laminate (force sensor). The sensor is then fabricated using the process outlined in *Section 2.1*. This general methodology was applied in the design and fabrication of the three repre-

sentative sensors presented in subsequent sections.

3.3   Transduction Mechanisms

Using printed-circuit MEMS fabrication, we have fabricated high-quality single/multi-axis force sensors using (a) custom foil-based strain gages, (b) light-intensity modulation (LIM), and (c) capacitance-based sensing.

3.3.1   Strain Gage Based Force Sensing

If we consider a serpentine gage with beam thickness t_g and width w_g, a normal strain ε along the gage axis results in a change in the beam's cross-sectional area $A = t_g w_g$ according to Poisson ratio ν. This is shown schematically in Fig. 5 (a). As the gage resistance R is linearly proportional to this cross-sectional area, we can ultimately measure this strain via a differential amplifier, as the resulting change in resistance can be linearly correlated with the input force.

The PCMEMS gage-based multiaxis force sensor exploits this transduction mechanism by employing a Maltese cross topology as shown in Fig. 5 (b) wherein four axisymmetric beams, each with two PCMEMS-manufactured serpentine-style metal foil strain gage (fabricated from high-resistivity Constantan foil, 5 μm thick) embedded in the laminate to measure both tension and compression of the beam, surround a central platform [20]. Each beam has a sensor configuration that comprises a half-bridge for thermal stability. A force applied to the central platform deforms each of the beams, and the strains measured by each half-bridge can be linearly combined to formulate a three-dimensional input force vector. The fabricated sensor prototype is shown in Fig. 5 (b).

As a practical demonstration, the sensor was attached to a robotic micromanipulation platform, and was used to palpate a biological tissue analog with high-stiffness intrusions embedded at various locations. The reconstructed tissue stiffness profile is shown in Fig. 5 (c), where black circles in the $x - y$ plane indicate the actual locations of the high-stiffness nodules (and the size indicates the relative depth), and the surface profile is reconstructed from discrete sensor measurements. The system was able to locate the nodules with an RMS error of less than 4 mm.

3.3.2   Light-Intensity Modulation

Exploiting self-assembly, a mm-scale uniaxial light-intensity-modulation force sensor is demonstratetd by integrating discrete emitter-detector pairs into a compliant structure designed to deform along the axis of the applied force [21]. Shown in Fig. 5 (d), the principle of light intensity modulation consists of an emitter and a detector are separated within a compliant structure by a distance $2h$. As a a force F is applied, the compliant structure deforms some distance δ_h, and the amount of irradiance reaching the detector increases according to a point-source intensity field model. If the emitter is a light-emitting diode (LED) and the detector is a phototransistor (PT), this change in distance manifests as an increase in collector current of the phototransistor which
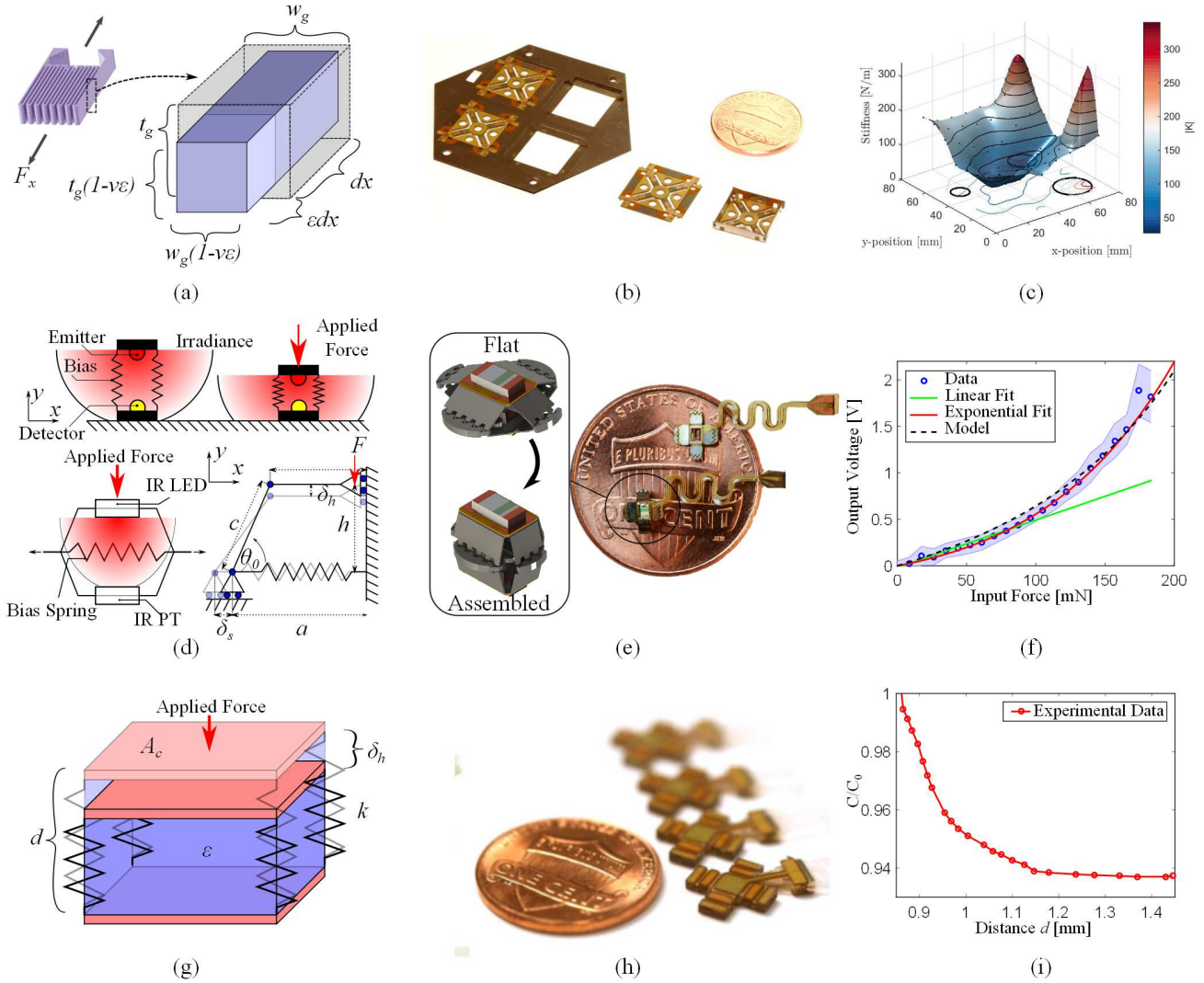
Fig. 5. Various transduction modalities demonstrated via PCMEMS: (a)-(c) strain gage-based force sensor modeling, fabricated prototype, and validation (reconstructed tissue stiffness profile obtained via robotic palpation), (d)-(f) light intensity modulation force sensor modeling, fabricated prototypes, and calibration profile, (g)-(i) capacitance force sensor modeling, fabricated prototype, and calibration profile.

can be easily converted into a voltage via simple amplification circuitry.

The PCMEMS LIM sensor is 'self-assembling' in that a pre-stretched planar spring is integrated into the laminate, which retracts when release cuts are made. The retraction of this spring actuates the fold patterns to transform the sensor from a flat, two-dimensional laminate into a boxy three-dimensional structure. Fiducials within the sensor allow for trivial pick-and-place assembly of electrical components (infrared LED and infrared PT). The fabricated sensor, shown in Fig. 5 (e), is 2.7mm in diameter, small enough to pass through the working channel of a commercial endoscope. The calibration curve in Fig. 5 (f) demonstrates that the sensor can sense forces in the range of hundreds of mN with high (0.8 mN) resolution.

3.3.3 Capacitance-Based Force/Position Sensing

The 'pop-up' capabilities of printed-circuit MEMS lend naturally to capacitance-based force/position sensing which, in its simplest form, consists of two parallel plates of area A_c separated by some distance d by a material with a dielectric constant ε_d and a stiffness k, shown schematically in Fig. 5 (g). As a force is applied, depressing the compliant material and bringing the plates closer together, the capacitance between the two plates changes, which can be measured.

Capacitance sensors were fabricated with a similar form factor to the LIM-based sensor, shown in Fig. 5 (h). Instead of a biasing spring, a novel manufacturing method was developed to enable the integration of thin elastomeric bladders within PCMEMS structure [22]. These bladders are filled with water to (a) assemble the sensor, (b) modulate the sensor stiffness which is proportional to the pressure in the bladder, and (c) improve the dielectric properties. The sensor, with the calibration curve shown in Fig. 5 (i), doubles as an actua-
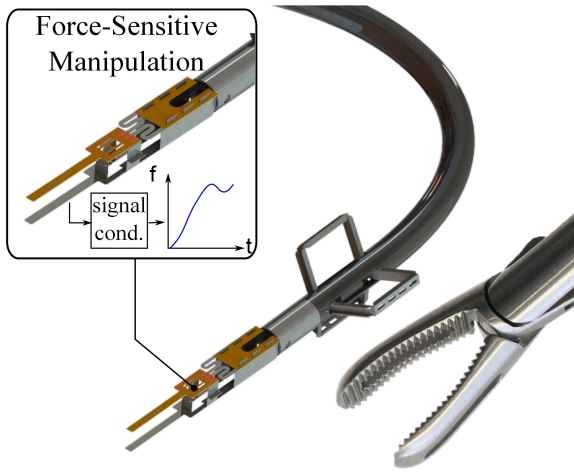
Fig. 6. Conceptual representation of force-sensing microsurgical forceps integrated into a flexible system, with an image of a conventional 5mm laparoscopic forcep for scale.
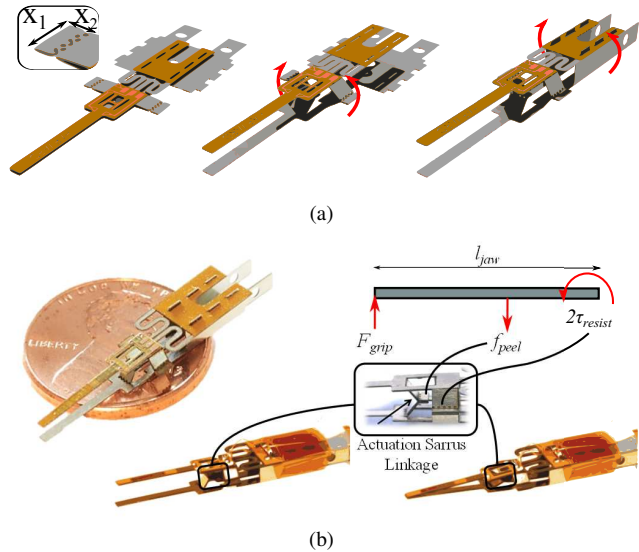

(a)

(b)

Fig. 7. (a) Origami-inspired assembly of force-sensing microsurgical forceps, (b) fabricated device on a US penny for scale and an associated kinematics diagram, showing internal Sarrus linkage and planar return spring.

tor with proprioceptive (position) sensing, as the elastomeric bladder can be pressurized by a hydraulic source to displace one plate with respect to the other, resulting in a mm-scale displacement-sensing linear actuator.

4 Mechanisms: Force-Sensing Micro-Forceps

Building upon work in PCMEMS fabrication of high resolution, compact sensors, a next step is to integrate PCMEMS sensing technology into a kinematic mechanism to demonstrate the potential for closed-loop force control at the millimeter scale. A particular strength of the technology is the ability to prescribe arbitrary kinematics to mechanical devices based on the placement of hinges, folding features and linkages in the laminate. Coupling sensing with linkages and mechanisms that can be actuated is a pivotal step towards fully on-board closed-loop control. To demonstrate this ability, we developed a force-sensing microforceps with potential force-reflection applications in microsurgery and minimally-invasive dexterous manipulation, as shown conceptually in Fig. 6.

4.1 Clinical Significance

Dexterous manipulation is of particular importance in microsurgical or intraluminal interventions, specifically in instances where the physician is manipulating delicate vasculature, or wants to separate a pathological specimen (tumor) from healthy tissue for resection and removal. Especially in cases where the tumor lies below the intraluminal surface (within the submucosal space), manipulation becomes extremely challenging from a clinical perspective when MIS techniques are employed. In such scenarios, a lack of haptic feedback can result in vessel rupture or damage to healthy tissue. As such, there is interest in developing sophisticated end-effectors capable of manipulating delicate tissue and providing information regarding the applied force.

Several groups have designed force-feedback forceps

for minimally-invasive and microsurgical applications by using commercial off-the-shelf strain sensors applied to flexural forcep elements [24, 25], sputtering strain gages onto commercial forceps and tweezers [26], or using fiber Bragg sensors manufactured into forcep jaws [27]. In general, sensorized end-effector design and fabrication is a challenge as numerous mm-scale heterogeneous components must be individually manufactured and hand-assembled. We present an alternative approach to force-sensing microforceps design by leveraging PCMEMS monolithic manufacturing to combine kinematics, sensing and actuation mechanisms in a single manufacturing step.

4.2 Forceps Design and Manufacturing

The gripper was manufactured using the same constituent materials as the multi-axis sensor (304SS for the mechanical substrate, Kapton polyimide for the flexure layers, FR1500 acrylic for the adhesive, and Constantan for the sensing element). The assembly of the gripper is facilitated by orthogonal Sarrus linkages, as well as tabs and slots, as shown in Fig. 7 (a). The mechanical actuation of the gripper is shown in Fig. 7 (b). All motion is permitted by flexure-based kinematics, using Kapton polyimide as the flexure layer. Two jaws are brought together by pulling at the midpoint of an internal Sarrus linkage as shown in the inset. A planar steel serpentine flexure deforms upon actuation, thus providing a restoring force which passively opens the grasper once the actuation force is removed. This flexure also supplies a counter-torque about the Sarrus linkage to close the jaws in a 'pinching' motion as shown in Fig. 7 (b). The closure kinematics can be arbitrarily selected by adjusting the distance between the flexure attachment point and the location of the internal Sarrus linkage, as well as adjust-
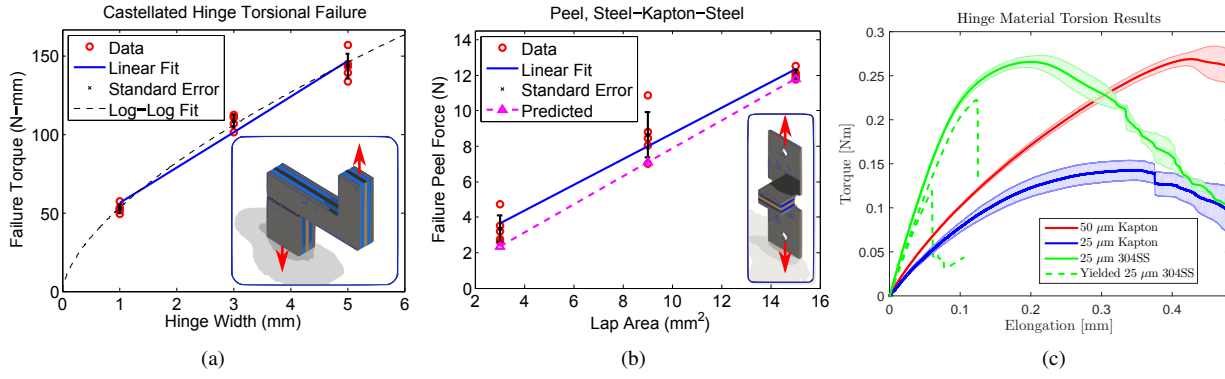
Fig. 8. (a) Torsion failure results and (b) peel failure results, both of which show a sufficiently linear dependence on hinge geometry, and insets show 3-D renderings of test samples, (c) torsion failure results for different hinge materials .*(a) and (b) re-printed with permission from ASME* [23].

ing the flexural stiffness of the return spring. Two external linkages act as rotary bearings to constrain any transverse motion between the jaws.

The grip load F_{grip} at the distal end of the jaws (of length l_{jaw}) is mechanically resisted by the torsional strength m_{resist} of the external linkages and the peel resistance f_{peel} of the internal Sarrus actuation linkage, as shown in Fig. 7 (b). We can use this knowledge to optimize the size of the linkage lap joints (areas where sublaminates are joined together by adhesive) subject to mechanical failure and size constraints. Prior hinge failure parametric studies (results of which are reproduced in Fig. 8 (a) and (b)) have shown that the Kapton-based flexural hinges have a torsional load resistance of $m_{resist} = 22.8 \pm 2.15 \mathrm{N} \cdot \mathrm{mm}$ per mm of hinge width (x_1) [23]. In addition, they have a peel load resistance of $f_{peel} = 0.72 \pm 0.10 \mathrm{N}$ per mm^2 of hinge lap area ($A_{lap} = x_1 \cdot x_2$, where x_2 is the lap tab width, refer to Fig. 7(a)). An additional constraint requires the hinge lap joints to be as small as possible to minimize the overall footprint of the device. As such, we have a nonlinear minimization problem where the objective is to minimize the hinge lap area $f(\mathbf{x}) = A_{lap}$ where $\mathbf{x} = (x_1, x_2)$ is the vector of free parameters:

$$\min (f(\mathbf{x})) = x_1 x_2 \qquad (2)$$

subject to the following constraints:

$$x_1 \geq \frac{F_{grip} l_{jaw}}{2 m_{resist}} \qquad (3)$$

$$x_2 \geq \frac{F_{grip}}{x_1 f_{peel}} \qquad (4)$$

This nonlinear, inequality-constrained optimization problem was solved in MATLAB using the fmincon() function given a design grip force of $F_{grip} = 1$ N and an initial
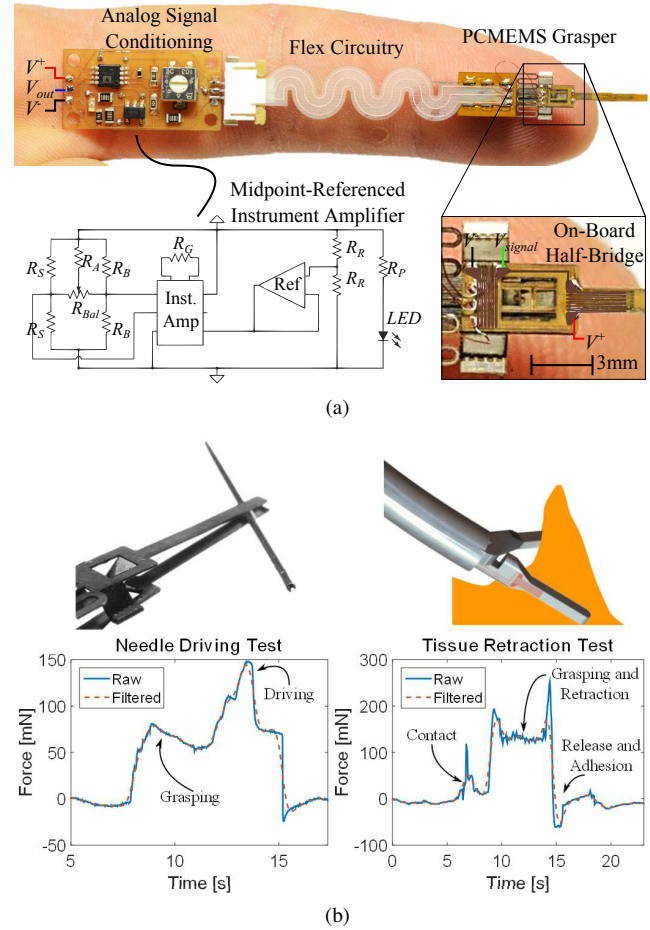

Fig. 9. (a) Force-sensing microsurgical forceps and associated wiring and signal conditioning, where the inset shows on-board half-bridge with the locations of the measuring and compensating gages highlighted, (b) *(left)* results of needle driving experiment showing a clear distinction between initial grip force and needle driving force, *(right)* results of tissue retraction experiment, where a number of discrete states (contact, grasping, retraction, and release) can be discerned based on the recorded force profile.

guess of $\mathbf{x} = (0.5, 0.5)$. The resulting hinge lap dimensions that generated a global minimum of the objective function

were $x_1 = 2.00$ mm and $x_2 = 0.70$ mm, resulting in a lap area of 1.39mm^2. These dimensions were implemented in the final gripper design.

The fabrication process is similar to that outlined in *Section 2.1* and shown in Fig. 2. The sensing mechanism is a half-bridge strain gage morphology implemented in the gripper mechanism, as shown in Fig. 9 (a). A custom signal conditioning circuit was developed, comprising a tunable half-bridge and a midpoint-reference instrumentation amplifier with adjustable gain.

4.3 Robustness Properties of Flexural Hinges

In addition to determining scaling laws for hinge geometry as presented in the previous section, we are also interested in exploring how different materials behave as hinges. We considered 25 μm and 50 μm Kapton, as well as 25 μm stainless steel. The torsional failure results for these three materials is shown in Fig. 8 (c). We see that very thin 304SS exhibits comparable torsional stiffness as a Kapton flexure with twice the thickness. However, the dotted green lines show the effects of fatigue on the steel (after the flexure hinge was bent 90 degrees, causing the hinge to plastically deform), wherein the torsional resistance is reduced drastically. Kapton-based flexure hinges have been shown to experience 10^6 loading cycles before failure [29]. Therefore, while steel hinges should primarily be used for assembly features (i.e. 'one-and-done'), Kapton is a good candidate for an active hinge material.

4.4 Validation: Open-Loop Needle Driving

Using a similar signal conditioning scheme as the multi-axis force sensor, the grip force sensor was calibrated by hanging discrete weights of known mass from the distal end of the grasper jaw and recording the resulting voltage. The sensor sensitivity was found to be roughly 4.8 V/N. The RMS noise of the sensor, measured by numerically integrating the power spectral density of a null signal measured over one minute, is roughly 23mV (corresponding to a force of 5 mN) setting a lower-bound on the sensor resolution.

A platform was built wherein the gripper is actuated manually by a cable attached to a trigger, and a real-time force reading is displayed by an LED bar graph where each bar represents 10 mN of force. In addition, force data is output to a serial port via an Arduino Nano microcontroller at a sample rate of 50Hz for real-time 10-bit analog force display and data post-processing.

To demonstrate the efficacy of the device in a clinical scenario, the gripper was used in a needle driving task and a tissue retraction task. In the needle driving task, the gripper manipulated a 19mm long, 1.5-gauge (m) straight-taper suture needle and drove it through a block of Ecoflex-0010. To simulate retraction, the gripper was used to peel a thin flap of Ecoflex-0010 from a larger continuum of the same material. The resulting force profiles generated from these tasks are shown in Fig. 9(b) (both raw and filtered with a 2nd order zero-phase Butterworth with a cutoff frequency of $\frac{\pi}{2}$ rad/sample). The results show that the force sensor is able

to detect forces with high signal-to-noise, and the differentiation between null force, grasping force and driving force is evident.

4.5 Validation: Robotic Micromanipulation

The gripper was also validated in a robotic micromanipulation platform consisting of a 3 orthogonally-mounted linear stages (Aerotech Inc., Pittsburgh, PA) to provide 3 DoF translational capabilities, a 2 DoF spherical 5-bar linkage to establish a remote center of motion, and 1 roll DoF. A custom module was fabricated to interface with the gripper which contained a 2.7 gram linear servo actuator and custom Wheatstone bridge-based signal conditioning PCB which was fastened to the distal end of the roll DoF, as shown in Fig. 10 (a). Using a Phantom Omni (Sensable, Wilmington, MA) as a master, the manipulation platform was used to assemble 14 1-mm diameter steel bearing balls into a 3-layered pyramid (Fig. 10 (b), while the gripper recorded the force required to pick up and displace the balls (Fig. 10 (c)). During the manipulation task the gripper measured 32.3 ± 3.08 mN of grip force required to pick up and displace the metal spheres [28].

Future work will entail the development a master system (based on Phantom Omni) with a custom haptic feedback module based on the integrated grip force measurement, and performing a user study with an appropriate tissue analog. This study will evaluate the efficacy of the force-sensing forceps in a grasping task by comparing the measured grip forces of the force-feedback system with conventional microsurgical tweezers.

5 Actuators: Distally-Actuated Cutting Device

The sensor and microforceps demonstrated the ability to couple kinesthetic force sensing with remotely-actuated kinematic mechanisms in a single monolithic fabrication process. The next component required for on-board loop closure is a means of coupling kinematics with distal actuators. As a demonstration of this component, we used PCMEMS to fabricate a high-frequency cutting tool with a flexural mechanism driven by on-board piezoelectric actuators. Such a device could realize a new generation of endoscope-based ultrasonic devices, wherein distally-implemented PZT transducers obviate the need for rigid tooling to transmit vibration energy from off-board actuators. In addition, on-board deflection sensing could enable real-time feedback control of cutting force and frequency, from which tissue parameters could be dynamically extracted [30].

5.1 Design, Modeling and Manufacturing

A kinematic representation of the device is shown in Fig. 11 (a), wherein a piezoelectric bimorph actuator forms one leg of a flexural four-bar linkage. The bimorph runs in parallel with a steel planar flexure which, in future iterations, could serve as the substrate for a PCMEMS strain sensor for real-time frequency feedback (leveraging methods used to develop the PCMEMS sensors discussed previously). As
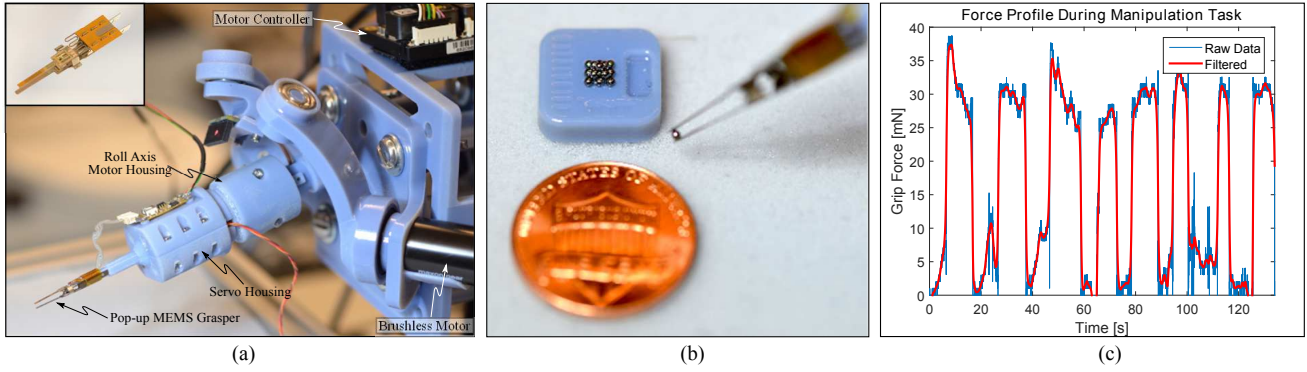
Fig. 10. Dexterous manipulation demonstration on a 6-DoF robotic micromanipulation platform, (a) robotic platform shown with gripper and modular servo/signal conditioning attachment, (b) still frame of gripper assembling a pyramid from 1mm steel bearing balls, and (c) representative force reading for 8 different ball displacements. *Reprinted with permission from IEEE* [28].
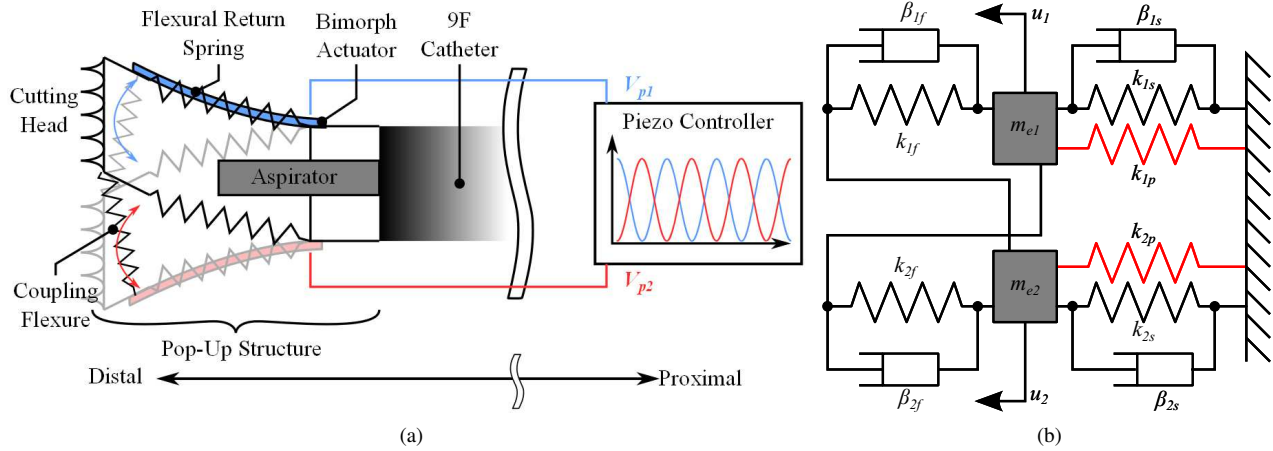

Fig. 11. (a) Kinematic representation of reciprocating cutting head and associated driving scheme, (b) mechanical representation of structural loop with relevant parameters.

the bimorph is energized, the bending along the length of the actuator results in an arc-like displacement of the cutting head which contains a plurality of micro-machined teeth. A similar actuator and four-bar mechanism is implemented on the bottom of the device which is driven 180 degrees out-of-phase with the previously-described actuator to create a reciprocating motion, wherein serrated jaws slide past one-another to shred tissue into fine particles which can be easily aspirated out of the body.

An analytical model of the system was built to ensure that the designed bimorph and flexure dimensions (1) would generate sufficient end-to-end differential displacement when driven at 200V, (2) exhibit quasi-static vibration characteristics (i.e. electrical response is much faster than mechanical response), and (3) have a combined resonant frequency of at least 10 times the operating frequency range of 50-100 Hz for mechanical stability. The system model was built by taking into consideration the constitutive behavior of the PZT actuator [31] (which can be used to obtain actuator stiffness k_p and the effective driven mass m_e), coupled with the second-order dynamics of the me-
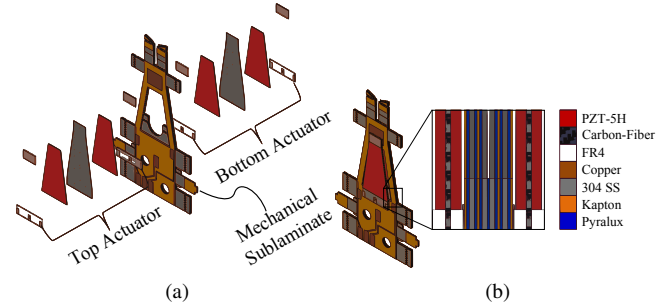

Fig. 12. Active cutting device manufacturing process: (a) exploded view of laminate, showing sublaminates for actuators and mechanisms, and (b) cross-section of the laminated structure.

chanical kinematic chain when modeled as a mass-spring-damper system as shown in Fig. 11 (b). The input to the system is this effective spring force exerted by the piezo ($k_p u$, denoted by the red spring), which is resisted by primary (Steel) and secondary (Kapton) flexural and damping forces which are themselves coupled between the two actuators. The electrical behavior of the actuator is modeled as
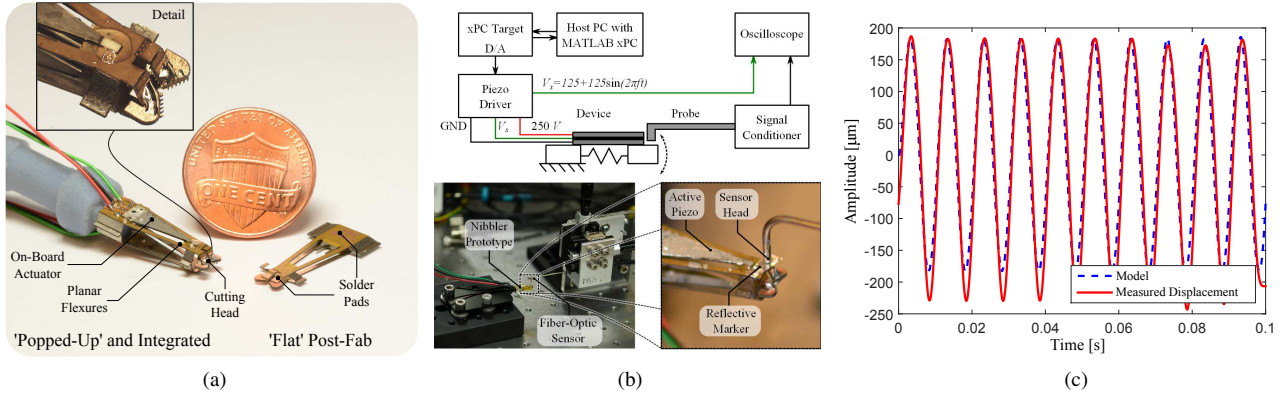
Fig. 13. (a) Fabricated tissue removal device actuated by on-board piezoelectric bimorphs, (b) test setup for kinematic evaluation of tissue cutting device, showing a detail of the sensor interface, and (c) testing results where the measured jaw displacement is compared with the displacement predicted by the dynamic model.

a lumped resistance/capacitance. By modifying the quasi-static model of a vibrating piezoelectric bimorph presented in [32] to include the added kinematics of the mechanical structure, we can determine the dynamic device behavior given an oscillating input voltage by solving a five-state model ($\mathbf{u} = [u_1, \dot{u}_1, u_2, \dot{u}_2, V_p]^T$) of system dynamics:

$$m_{e1}\frac{d u_1^2}{d^2 t} = (k_{1s} - k_{1p})u_1 + k_{1f}(u_1 - u_2)$$
$$+ \beta_{1s}\frac{du_1}{dt} + \beta_{1f}\left(\frac{du_1}{dt} - \frac{du_2}{dt}\right) + \Theta V_p \tag{5}$$

$$m_{e2}\frac{d u_2^2}{d^2 t} = (k_{2s} - k_{2p})u_2 + k_{2f}(u_2 - u_1)$$
$$+ \beta_{2s}\frac{du_2}{dt} + \beta_{2f}\left(\frac{du_2}{dt} - \frac{du_1}{dt}\right) + \Theta V_p \tag{6}$$

$$\frac{dV_p}{dt}C_f + V_p\left(\frac{1}{R_0 + R_l}\right) = \frac{V_s}{R_l} \tag{7}$$

where $m_{e1,2}$ are the effective driven masses, $u_{1,2}$ are the end deflections, $\beta_{1f,2f}$ is the damping in the flexure hinges, $\beta_{1s,2s}$ is the squeeze film damping, $k_{1s,2s}$ are the primary steel flexure stiffnesses, $k_{1p,2p}$ are the piezo stiffnesses, $k_{1f,2f}$ are the secondary Kapton flexure stiffnesses, Θ is the voltage coupling constant of PZT, V_p is the voltage across the PZT, R_0 is the dielectric impedance, and R_l is the lead resistance. Solving the equations for a target 200 V sine wave at 100 Hz (an upper bound on the driving frequency) results in a differential displacement of nearly 500 μm. Additionally, the electromechanical dynamics of the actuator respond much faster than the input drive frequency (with a rise time of 1.3 μs), satisfying the quasi-steady vibration condition for which the analytical model is valid.

5.2 Manufacturing

An exploded view of the CAD-generated device laminate is shown in Fig. 12. Custom piezoelectric bimorph actuators are made in-house using a composite lamination process wherein two 125 μm lead zirconate titanate (PZT5H) piezoelectric plates, one 87 μm pre-cured carbon fiber laminate, and two 125 μm Copper-cladded FR4 dielectric layers are machined using a DPSS laser and laminated together using a precision alignment and lamination process. After testing the actuators for proper operation, they are then placed into the mechanical sublaminate using kinematic alignment features, and conductive epoxy is used for both mechanical fastening and transmission of electrical signals from traces on the mechanical sublaminate to contacts on the actuators. The mechanical sublaminate is manufactured using a separate PCMEMS process similar to that used for the microsurgical forceps. A layer of polyimide insulates the PZT from the stainless steel structure of the device. The finished device, shown integrated with a 3D-printed coupling for debris aspiration, is shown in Fig. 13(a).

5.3 Kinematic Validation

To verify the kinematics, an experiment was performed wherein the top-side piezo actuator was energized with a 250 V_{pp} sinusoid at a number of frequencies ranging from 1-100 Hz. The resulting tip displacement was measured via a fiber-optic displacement sensor (Philtec D21) operating in the near field (with an output sensitivity of 3 mV/μm). An image of the testing setup is shown in Fig. 13 (b).

Example results for a 100 Hz drive signal are shown in Fig. 13 (c). The overall displacement of a single actuator is $\pm 200 \mu$m, meaning the overall differential displacement between two actuators oscillating out-of-phase is $\sim 400 \mu$m. The model closely fits (but underpredicts) the overall displacement of the active jaw.

Although the device could generate enough force to debride a blood clot analog (gelatin), when tested against a muscular tissue analog (porcine intestine), the reaction force from the tissue was greater than the blocking force of the
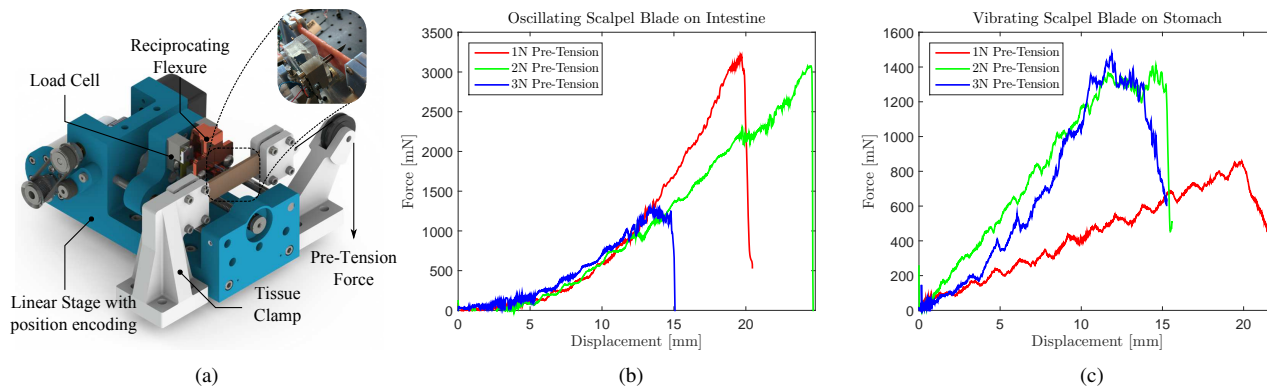
Fig. 14. Mechanical Debridement Results: (a) Test setup (inset shows blade penetrating tissue), (b) force/displacement curve for oscillating blade on pig intestine, (c) force/displacement curve for oscillating blade on pig stomach.

Table 1. PCMEMS Material Biocompatibility (actuator subsystems consider net biocompatibility of all constituent components)

Sensors/Electronics	BC	Actuators	BC	Structural Materials	BC	Transfer Adhesives	BC
Constantan	(-)	Piezo-Ceramics	(+)	304SS	(+)	FR1500 Adhesive	(*)
Karma Alloy	(-)	Shape-Memory Alloy	(+)	Spring Steel	(+)	FR0100 Adhesive	(*)
Copper	(-)	Elastomeric Pneumatic	(+)	Titanium	(+)	3M 1504	(+)
Discrete IC	(*)	Lorentz Coil [33]	(0)	6061-T6 Aluminum	(+)	3M 1524	(+)
Nickel-Chromium	(0)	Electrostatic	(+)	Parylene C	(+)		
Gold	(+)			Kapton Polyimide	(+)		
Platinum	(+)			FR4	(+)		
Sn-Pb Solder	(-)			Nitinol	(+)		
Pb-free Solder	(+)			Carbon Fiber	(+)		

piezo actuators (which is typically on the order of 200-500 mN), causing the oscillating blade to 'jam'. To determine the required cutting force to mechanically debride tissue of this nature, a test platform was constructed (Fig. 14 (a)) consisting of a linear stage with position encoding, and a 3D-printed flexure which transmits vibratory motion from a DC vibration motor to a cutting blade, thereby 'approximating' the cutting action of the piezo-driven device. The reaction force is measured via a load cell that is in-line with the flexure. The tissue is clamped and pre-tensioned by a known weight, the blade (oscillating at the design frequency of 100 Hz) is pressed into the tissue, and the reaction force is recorded up until complete penetration. As the results show in Fig. 14 (b) and (c), the required cutting force for gastrointestinal tissue analog can be as high as 3N depending on the amount of tissue pre-tension. These results show that piezo bimorph-driven cutting tools may not be appropriate for debriding muscular tissue as the force output simply is not sufficient. As a result of these tests, we are actively exploring actuation methods with higher blocking force (piezo stack actuators) for mechanical debridement. In terms of soft tissue cutting, driving actuators at ultrasonic frequencies (50 kHz and higher) results in protein denaturation of tissue with the

added benefit of coagulation, and as such, does not rely on substantial cutting forces which are generally difficult to generate on board flexible tooling.

6 Persisting Challenges

PCMEMS is a very promising approach to fabricating millimeter scale end-effectors for flexible surgical robotic systems. However, there remain a number of technical challenges that will be addressed in future work to further establish the technique as a clinically viable manufacturing solution.

6.1 Biocompatibility:

A unifying challenge facing every medical device designer is ensuring that all constituent materials are biocompatible. Despite the expansive material catalog leveraged by PCMEMS, several constituent materials are themselves biologically incompatible. Tested materials that are compatible with the PCMEMS process, as well as their biocompatibilities, are summarized in Table 1 (where (-) = major cytotoxicity effects, (0) = minor cytoxicity effects over short duration,

(+) = biocompatible, and (*) = untested). Many sensor component materials themselves are directly incompatible as can be seen, especially materials used for electrical conductors and traces such as copper and constantan. Although not ideal from a cost perspective, it is possible to electroplate copper traces using precious metals such as gold and platinum, or use a sputter-coating process to manufacture biocompatible circuit traces and contacts using these precious metals directly. In addition, it is possible to encapsulate these materials in Parylene C which has been shown to be a viable biocompatible encapsulant for numerous PCB materials including copper, nickel and FR4 [34]. As Parylene C itself is an inextensible (but flexible) polymer, applying a thin coating of the material after release does not significantly affect the kinematics of PCMEMS mechanisms which primarily rely on the bending mode of embedded flexures for movement.

6.2 Robustness:

The use of thin layers of materials brings about obvious concerns of robustness, as device stiffness scales with the cube of the laminate thickness. We address this problem by including non-planar features (i.e. hinges that fold and lock out-of-plane, pick-and-place strut features) that serve to augment the bending moment of the respective structures (an example being the foldable struts in the multi-axis force sensor) We briefly addressed the issue of hinge robustness in *Section 4.3*, however, much work remains to be done in expanding the catalog of appropriate hinge materials and analyzing their flexural properties.

6.3 Continuous Motion:

Many medical devices leverage continuous rotary motion, as in mechanical debriders, motorized burrs and shavers. Achieving continuous rotary motion has not been demonstrated using PCMEMS, as the motion-permitting flexures are inherently limited in stroke. As a result, devices must be designed under the constraint of limited-stroke or reciprocating motion.

6.4 Soft Encapsulation:

The use of thin metallic alloys for substrate materials can result in sharp edges and pinch points that (a) can be difficult to sterilize and (b) pose as perforation/puncture risks to delicate anatomy. As such, we are actively exploring ways to marry PCMEMS with the field of soft robotics to combine the merits of mesoscale manufacturing and soft materials and produce devices that interact with biological anatomy in an inherently safe manner.

7 Conclusions

This paper summarizes knowledge gained from preliminary demonstrations of prototypical medical devices with integrated mechanisms, sensors and actuators fabricated using a disruptive manufacturing process inspired by printed circuit board processing. By exploiting the inherent ability to integrate and couple mechanisms, sensors and actuators in a monolithic way, we can side-step the limitations imposed by conventional manufacturing approaches to enable low-cost fabrication of smarter tooling for task-specific medical co-robotic devices. Bench-level validations have shown that this fabrication technique is feasible for creating robotic end-effectors that are compatible with form-factors imposed by minimially-invasive surgery. We have also discussed practical limitations that stand between the current state of the technology and clinical viability. Future efforts will focus on addressing these limitations, in addition to solving technical challenges such as integration of the disparate modules demonstrated herein to realize a 'smart' mm-scale end-effector modules with applications in flexible endoscopic and catheter-based procedures. We will explore areas that are of particular importance to the endoscopic community, including tissue retraction, endoscope stabilization, and alternative methods of tissue removal. The ultimate goal of this work is to enable low-cost, modular add-ons to existing endoscopic equipment that will augment a clinicians ability to perceive and manipulate tissue minimally-invasively.

References

[1] Sedel, L., Nizard, R., and Meunier, A., 1995. "Orthopedic biomaterials". *Bulletin de l'Academie nationale de medecine,* **179**(3), pp. 497–505; discussion 505–506.

[2] Dupont, P. E., Lock, J., Itkowitz, B., and Butler, E., 2010. "Design and Control of Concentric-Tube Robots". *IEEE Transactions on Robotics,* **26**(2), pp. 209–225.

[3] Weaver, K., Webster, R., Swaney, P., Burgner, J., Russell, P., Gilbert, H., Bekeny, J., and Hendrick, R., 2013. "The Use of Teleoperated Concentric Tube Robots for Transsphenoidal Parasellar Surgery". *Journal of Neurological Surgery Part B: Skull Base,* **74**(S 01), p. A123.

[4] Webster, R. J., 2007. "Design and Mechanics of Continuum Robots for Surgery". *Russell The Journal Of The Bertrand Russell Archives,* **29**(13), pp. 1661–1683.

[5] Bajo, A., Dharamsi, L. M., Netterville, J. L., Garrett, C. G., and Simaan, N., 2013. "Robotic-Assisted Micro-Surgery of the Throat : the Trans-Nasal Approach". *IEEE International Conference on Robotics and Automation*, pp. 232–238.

[6] Simaan, N., Kai Xu, Wei Wei, Kapoor, A., Kazanzides, P., Taylor, R., and Flint, P., 2009. "Design and Integration of a Telerobotic System for Minimally Invasive

Surgery of the Throat". *The International Journal of Robotics Research,* **28**(9), pp. 1134–1153.

[7] Kesner, S. B., and Howe, R. D., 2014. "Robotic catheter cardiac ablation combining ultrasound guidance and force control". *The International Journal of Robotics Research,* **33**(4), pp. 631–644.

[8] Schneider, J., Burgner, J., Webster III, R., and Russell III, P., 2014. "Robotic surgery for the sinuses and skull base: What are the possibilities and what are the obstacles?". *Curr Opin Otolaryngol Head Neck Surg,* **21**(1), pp. 11–16.

[9] Gosline, A., Vasilyev, N., Veeramini, A., Wu, M., Schmitz, G., Chen, R., Arabagi, V., del Nido, P., and Dupont, P., 2012. "Metal MEMS Tools for Beating-heart Tissue Removal". *IEEE International Conference on Robotics and Automation*, pp. 1921–1926.

[10] Rebello, K. J., 2004. "Applications of MEMS in surgery". In Proceedings of the IEEE, Vol. 92, pp. 43–55.

[11] Traeger, M. F., Roppenecker, D. B., Leininger, M. R., Schnoes, F., and Lueth, T. C., 2014. "Design of a spine-inspired kinematic for the guidance of flexible instruments in minimally invasive surgery". *2014 IEEE/RSJ International Conference on Intelligent Robots and Systems*(Iros), pp. 1322–1327.

[12] Whitney, J. P., Sreetharan, P. S., Ma, K. Y., and Wood, R. J., 2011. "Pop-up book MEMS". *Journal of Micromechanics and Microengineering,* **21**(11), p. 115021.

[13] Bethea, B., Okamura, A., Kitagawa, M., Fitton, T., Cattaneo, S., Gott, V., Baumgartner, W., and Yuh, D., 2005. "Application of Haptic Feedback to Robotic Surgery". *J Laparoendosc Adv Surg Tech A,* **14**(3), pp. 191–195.

[14] Moradi Dalvand, M., Shirinzadeh, B., Nahavandi, S., Karimirad, F., and Smith, J., 2013. "Force Measurement Capability for Robotic Assisted Minimally Invasive Surgery Systems". *International Conference on Intelligent Automation and Robotics (ICIAR),* **I**, pp. 419–424, Best Paper Award.

[15] Trejos, A., Patel, R., and Naish, M., 2010. "Force sensing and its application in minimally invasive surgery and therapy: a survey". *Proceedings of the Institution of Mechanical Engineers, Part C: Journal of Mechanical Engineering Science,* **224**(7), pp. 1435–1454.

[16] Polygerinos, P., Zbyszewksi, D., Schaeffter, T., Razavi, R., Seneviratne, L., and Althoefer, K., 2010. "MRI-Compatible Fiber-Optic Force Sensors for Catheterization Procedures". *Sensors Journal, IEEE,* **10**(10), pp. 1598–1608.

[17] Sun, Z., Balicki, M., Kang, J., Handa, J., Gehlbach, P., and Iordachita, I., 2010. "NIH Public Access". *International Journal,* **4**(April 2009), pp. 1–20.

[18] Park, Y. L., Chau, K., Black, R. J., and Cutkosky, M. R., 2007. "Force sensing robot fingers using embedded fiber Bragg grating sensors and shape deposition manufacturing". In Proceedings - IEEE International Conference on Robotics and Automation, pp. 1510–1516.

[19] Puangmali, P., Liu, H., Seneviratne, L. D., Dasgupta,

P., and Althoefer, K., 2012. "Miniature 3-axis distal force sensor for minimally invasive surgical palpation". *IEEE/ASME Transactions on Mechatronics,* **17**(4), pp. 646–656.

[20] Gafford, J. B., Kesner, S. B., Degirmenci, A., Wood, R. J., Howe, R. D., and Walsh, C. J., 2014. "A Monolithic Approach to Fabricating Low-Cost , Millimeter-Scale Multi-Axis Force Sensors for Minimally-Invasive Surgery". In Robotics and Automation (ICRA), 2014 IEEE International Conference on, pp. 1419–1425.

[21] Gafford, J. B., Wood, R. J., and Walsh, C. J., 2016. "Self-assembling, low-cost, and modular mm-scale force sensor". *IEEE Sensors Journal,* **16**(1), Jan, pp. 69–76.

[22] Russo, S., Ranzani, T., Gafford, J., Walsh, C. J., and Wood, R. J., 2016. "Soft pop-up mechanisms for micro surgical tools: Design and characterization of compliant millimeter-scale articulated structures". In 2016 IEEE International Conference on Robotics and Automation (ICRA), pp. 750–757.

[23] Gafford, J. B., Wood, R. J., Kesner, S. B., and Walsh, C. J., 2013. "Microsurgical Devices by Pop-Up Book MEMS". In ASME 2013 International Design Engineering Technical Conferences and Computers and Information in Engineering Conference, pp. 1–7.

[24] Payne, C. J., Rafii-Tari, H., Marcus, H. J., and Yang, G. Z., 2014. "Hand-held microsurgical forceps with force-feedback for micromanipulation". In Proceedings - IEEE International Conference on Robotics and Automation, pp. 284–289.

[25] Menciassi, A., Eisinberg, A., Carrozza, M. C., and Dario, P., 2003. "Force sensing microinstrument for measuring tissue properties and pulse in microsurgery". In IEEE/ASME Transactions on Mechatronics, Vol. 8, pp. 10–17.

[26] Hammond III, F., Smith, M., and Wood, R., 2014. "Printing strain gauges on surgical instruments for force measurement.". *J Med Devices,* **8**(3).

[27] Lim, S.-C., Lee, H.-K., and Park, J., 2014. "Grip force measurement of forceps with fibre Bragg grating sensors". *Electronics Letters,* **50**(10), pp. 733–735.

[28] Degirmenci, A., Hammond, F., Gafford, J. B., Walsh, C. J., Wood, R. J., and Howe, R. D., 2015. "Design and Control of a Parallel Linkage Wrist for Robotic Microsurgery". In Intelligent Robots and Systems (IROS), 2015 IEEE/RSJ International Conference on, pp. 222–228.

[29] Malka, R., Desbiens, A. L., Chen, Y., and Wood, R. J., 2014. "Principles of microscale flexure hinge design for enhanced endurance". In IEEE International Conference on Intelligent Robots and Systems, no. Iros, pp. 2879–2885.

[30] Lopez, J., Kang, I., You, W., McDonald, D., and Weaver, V., 2011. "In situ force mapping of mammary gland transformation.". *Integr Biol (Camb).,* **3**(9), pp. 910–921.

[31] Wood, R., Steltz, E., and Fearing, R., 2005. "Optimal energy density piezoelectric bending actuators". *Sen-*

sors and Actuators A: Physical, **119**(October 2004), pp. 476–488.

[32] Tabesh, A., and Fréchette, L. G., 2008. "An improved small-deflection electromechanical model for piezoelectric bending beam actuators and energy harvesters". *Journal of Micromechanics and Microengineering,* **18**(10), p. 104009.

[33] Goldberg, B., Karpelson, M., Ozcan, O., and Wood, R. J., 2014. "Planar fabrication of a mesoscale voice coil actuator". In Proceedings - IEEE International Conference on Robotics and Automation, pp. 6319–6325.

[34] Bellmann, C., Beshchasna, N., Uhlemann, J., and Wolter, K. J., 2009. "Parylene C and silicone as biocompatible protection encapsulants for PCBs". In ISSE 2009: 32nd International Spring Seminar on Electronics Technology: Hetero System Integration, the path to New Solutions in the Modern Electronics - Conference Proceedings.